**Hydrology and
Earth System
Sciences
Discussions**

Pattern dynamics, pattern hierarchies, and forecasting in complex multi-scale earth systems

J. B. Rundle[1,2]**, D. L. Turcotte**[3]**, P. B. Rundle**[1,2]**, G. Yakovlev**[2]**, R. Shcherbakov**[2]**,
A. Donnellan**[4]**, and W. Klein**[5]

[1]Department of Physics, University of California, Davis, CA, USA
[2]Computational Science and Engineering Center, University of California, Davis, CA, USA
[3]Geology Department, University of California, Davis, CA, USA
[4]Earth and Space Science Division, Jet Propulsion Laboratory, Pasadena, CA, USA
[5]Department of Physics, Boston University, Boston, MA, USA

Correspondence to: J. B. Rundle (jbrundle@ucdavis.edu)

Title Page

Abstract | Introduction

Conclusions | References

Tables | Figures

|◄ | ►|

◄ | ►

Back | Close

Full Screen / Esc

Printer-friendly Version

Interactive Discussion

EGU

Pattern dynamics, pattern hierarchies, and forecasting

J. B. Rundle et al.

Abstract

Catastrophic disasters afflicting human society are often triggered by tsunamis, earthquakes, widespread flooding, and weather and climate events. As human populations increasingly move into geographic areas affected by these earth system hazards, forecasting the onset of these large and damaging events has become increasingly urgent. In this paper we consider the fundamental problem of forecasting in complex multi-scale earth systems when the basic dynamical variables are either unobservable or incompletely observed. In such cases, the forecaster must rely on incompletely determined, but "tunable" models to interpret observable space-time patterns of events. The sequence of observable patterns constitute an apparent pattern dynamics, which is related to the underlying but hidden Newtonian dynamics by a complex dimensional reduction process. As an example, we examine the problem of earthquakes, which must utilize current and past observations of observables such as seismicity and surface strain to produce forecasts of future activity. We show that numerical simulations of earthquake fault systems are needed in order to relate the fundamentally unobservable nonlinear dynamics to the readily observable pattern dynamics. We also show that the space-time patterns produced by the simulations lead to a scale-invariant hierarchy of patterns, similar to other nonlinear systems. We point out that a similar program of simulations has been very successful in weather forecasting, in which current and past observations of weather patterns are routinely extrapolated forward in time via numerical simulations in order to forecast future weather patterns.

1 Introduction

The critical need to forecast natural hazards has been underscored by the 26 December 2004 M~9.3 Sumatra earthquake and tsunami that led to the deaths of more than 275 000 persons (Lay et al., 2005[1]); Hurricane Katrina, a category 5 storm that weak-

---

[1] http://earthquake.usgs.gov/eqinthenews/2004/usslav/

ened to a category 3 storm before flooding New Orleans and the Gulf Coast of the United States on August 29, 2005, causing as much as \$130 billion in damages and killing more than 1000 persons (J. Travis, 2005[2]); and the M~7.6 Pakistan earthquake of 8 October 2005 with estimated fatalities of more than 87 000 persons[3]. Secondary
5 disasters can also occur such as landslides, flooding, and tornadoes.

Given the spatial scales of these events, and the rapid onset of their most severe effects, the development of a physics-based understanding of these hazards must be a high priority, especially since human populations are increasingly moving into the areas most likely to be affected by these disasters. A physical understanding of these
10 dynamical processes leads to the possibility of forecasting and prediction, based upon the use of numerical simulations, similar to the methods by which progress has been made in the field of weather and climate forecasting during the past few decades.

Earthquakes are an example of a threshold system, in which the stress on a fault increases persistently due to plate tectonic forces. In general, driven nonlinear threshold
15 systems are comprised of interacting spatial networks of statistically identical, nonlinear units or cells that are subjected to a persistent driving force or current. A cell "fires" or "fails" when the force, electrical potential, or other physical variable $\sigma(\boldsymbol{x}, t)$ in a cell at position $\boldsymbol{x}$ and time t reaches a predefined force threshold σ^F. The result is an increase in an internal state variable $s(\boldsymbol{x}, t)$ of the cell, as well as a decrease in the force
20 or potential sustained by the cell to a residual value σ^R. Thresholds, residual stresses, and internal states may be modified by the presence of quenched disorder, and the dynamics also may be modified by the presence of noise or disorder. Interactions between cells may be excitatory (positive) in the sense that failure of connected neighbors brings a cell closer to firing, or inhibiting (negative) in the opposite case.
25 In the case of earthquake fault systems, the cell or site represents a location $\boldsymbol{x}$ on a fault; the state variable $\sigma(\boldsymbol{x}, t)$ represents the stress; the force threshold σ^F is the static frictional strength; and the residual value σ^R is the fault stress at the conclusion

---

[2]http://www.nhc.noaa.gov/archive/2005/tws/MIATWSAT_aug.shtml
[3]http://earthquake.usgs.gov/recenteqsww/Quakes/usdyae.htm

Pattern dynamics, pattern hierarchies, and forecasting

J. B. Rundle et al.

EGU

of sliding. In earthquake fault systems, the fault slips when the static frictional threshold is reached, in a process that reduces the stress to a lower, residual value. As a result of the earthquake, a portion of the stress is lost during the event, and the remainder is redistributed to other faults and regions in the system. If the redistributed stress

5 leads to a state of supercritical stress on other faults, an avalanche of triggered failures may occur, increasing the magnitude of the earthquake. Other examples of threshold systems are common in nature, and include the occurrence of floods in river networks, landslides, volcanic eruptions, ecological systems, saturation and soil moisture, and biological epidemics. Threshold systems are also seen in other science and engineering

10 applications, such as depinning transitions in charge density waves and superconductors, magnetized domains in ferromagnets, sandpiles, and foams (Rundle et al., 2000, 2002). As another example, for neural networks a cell is a neuron, $\sigma(\boldsymbol{x}, t)$ represents the cellular electrical potential, σ^F is the firing potential, and σ^R is the potential after the cell discharges.

15 The failure of the levees when Hurricane Katrina struck New Orleans was also an example of a threshold process. Here the large amounts of rainfall and the storm surges led to overfilling of Lake Ponchartrain and the catastrophic failure of the levee system that protected the sections of the city lying below sea level.

Both weather and seismicity are complex, chaotic phenomena. Current weather pat-

20 terns are routinely extrapolated forward in order to forecast the weather several days into the future. These forecasts utilize numerical simulations of atmospheric behavior. A specific example concerns the future tracks of hurricanes. The standard approach is to utilize ensemble forecasting. Forecasts are made using a variety of numerical simulations. If these simulations converge on similar tracks, then the forecast is considered

25 robust. The question is whether a similar approach can be developed for earthquake forecasting, and whether it can then be extended to other driven systems common in geomorphology and hydrology.

2   Patterns in El Nino events

Among the fields of research that have recently made significant progress in recognizing, interpreting, and predicting such patterns are weather forecasting, specifically predictions in the onset of El Nino-Southern Oscillation events. These methods utilize variations of Principal Component Analysis, Principal Oscillation Pattern Analysis, and Singular Spectrum Analysis (Preisendorfer, 1988; Penland, 1989; Penland and Sardeshmukh, 1995; Penland and Mangorian, 1993; Broomhead and King, 1986; Vautard and Ghil, 1989). Prediction of pattern development and evolution is complicated by the presence of noise, nonlinear mode interactions, and a variety of other factors, but progress has been made in recent years as exemplified by the successful prediction of the El Nino weather event of 1998. In most of these methods, it is assumed that the observed time series have Markov characteristics, so that the observed state of the system at time $t+\Delta t$ depends only on the observed state of the system at time t. There are typically many time scales in the dynamics, some of which can be as small as Δt, and others that can be much longer.

However, in making El Nino forecasts for a year in advance, it is typical to focus on processes, such as sea surface warming off the Pacific coast of South America, that take place over the preceeding weeks to months. This assumption of a relatively small range in time scale evidently holds reasonably well for El Nino events.

An additional important assumption made by some investigators is that the space-time patterns of El Nino events can be considered to be described by a linear stochastic equation (Penland and Matrosova, 2006; Penland and Sardeshmukh, 1995), which is used to forecast the future occurrence and evolution of El Nino events. In this procedure, which we summarize briefly here, the evolution of tropical sea surface temperature (SST) anomaly $\theta(\boldsymbol{x},t)$ is represented as a stable linear process maintained by a stochastic forcing $\eta(\boldsymbol{x},t)$:

$$\frac{\partial \theta(\boldsymbol{x},t)}{\partial t} = \boldsymbol{B}\,\theta(\boldsymbol{x},t) + \eta(\boldsymbol{x},t) \qquad (1)$$

EGU

In these types of applications, the function $\theta(\boldsymbol{x}, t)$, which depends on coarse-grained locations centered at $\boldsymbol{x}$, is considered to be a vector in a Hilbert space (see, e.g., Jordan, 1969). $\theta(\boldsymbol{x}, t)$ has all the usual properties of vectors, including a metric and a well defined algebra.

5   In Eq. (1), $\boldsymbol{B}$ is assumed to be a linear operator that is non-normal, meaning that its eigenvectors $E_i(\boldsymbol{x})$ are non-orthogonal. The eigenvectors evolve at different rates, and interfere with each other in such a way that, when the initial El Nino anomaly projects strongly onto an "optimal" initial pattern state, the spatial variance of the temperature anomaly field, representing the El Nino event, then increases to a maximum (Farrell,

10   1988). The eigenvectors of $\boldsymbol{B}$ are assumed to be complete, so that the actual SST anomaly $\theta(\boldsymbol{x}, t)$ at any time can be represented as a linear sum of the eigenvectors $E_i(\boldsymbol{x})$:

$$\theta(\boldsymbol{x}, t) = \sum_{i=1}^{N} \alpha_i(t)E_i(\boldsymbol{x}) \tag{2}$$

The corresponding pattern evolution operator P(t) is found by formally integrating the
15   dynamical Eq. (1), setting the stochastic forcing $\eta(\boldsymbol{x}, t)=0$:

$$P(t) = e^{Bt} \tag{3}$$

Note that in this case, the Eq. (1) does not represent the fundamental equations that govern the SST anomoly, it is rather a simple linear stochastic equation that is assumed to govern the evolution of the space-time patterns associated with El Nino events.

20   Moreover, the pattern evolution operator P(t) is not known a priori, it must instead be determined from data, or from theoretical considerations. An advantage is that SST anomalies can be directly observed via satellite observations, and the El Nino cycles are sufficiently short (~6 years) that time series techniques can be used to filter and isolate the important SST signals.

EGU

3   Threshold systems

Driven threshold systems are complex systems that are characterized by both sudden observable events, such as earthquakes, as well as an underlying Newtonian dynamics that is largely unobservable, as well as being subject to unobservable stochastic perturbations. It is important to note that the events do not represent the true dynamics that governs evolution of the system, they are only a product of the dynamics. Examples of such systems include not only earthquakes, but also landslides and avalanches, floods, and other non-geological systems including neural networks, and magnetic depinning transitions in superconductors. In these cases, the observable events are impulsive phenomena that are the result of the persistent forcing of the underlying dynamics (Rundle et al., 2000). While the time scale for the forcing is often relatively long, the time scale for the observable events is usually short. Since we cannot observe the underlying dynamics, we usually have no choice but to interpret, and to try to forecast, the evolution of the system on the basis of the observable events. We are therefore led to define a state vector $S(\boldsymbol{x}, t)$ representing the rate of occurrence of the impulsive events within a small, coarse-grained region centered on the location $\boldsymbol{x}$ (Rundle et al., 2000). One example of such a coarse-graining would be to cover a geographic area such as southern California with a lattice of small regions (boxes) of a certain small size, for example boxes of size .1˚ (Lattitude) by .1˚ (Longitude). This procedure has been carried out in recent work on earthquake forecasting (Holliday et al., 2006). For the simulations we discuss below, $\boldsymbol{x}$ represents the location of the center of a fault segment. For these simulations, $S(\boldsymbol{x}, t)$=1 if the segment slips at time t, and zero otherwise (Rundle et al., 2000). For observed data, $S(\boldsymbol{x}, t)$ may have any real integer value at time t.

For threshold systems driven at a constant rate, systems that are large compared to the spatial scale of the impulsive events can often be considered to execute small fluctuations around a steady state. This assumption has been shown to hold for earthquakes (Turcotte, 1997; Tiampo et al., 2003).

If we regard the system state $S(\boldsymbol{x}, t)$ as representing the real part of a complex-

valued function $\psi(\boldsymbol{x}, t)$, then we have shown in previous work (Rundle et al., 2000) that $\psi(\boldsymbol{x}, t)$ can be written as:

$$\Psi(t) = \psi(\boldsymbol{x}, t) = \sum_{n=1}^{N} \alpha_n \, e^{i \, \omega_n t} \, \phi_n(\boldsymbol{x}) \tag{4}$$

where the $\phi_n(\boldsymbol{x})$ are eigenfunctions, or "eigenpatterns", the ω_n are eigenfrequencies, N is the number of coarse-grained regions or boxes, and the expansion coefficients α_n satisfy the constraint:

$$\sum_{n=1}^{N} |\alpha_n|^2 = 1 \tag{5}$$

The notation $\Psi(t) = \psi(\boldsymbol{x}, t)$ emphasizes that $\psi(\boldsymbol{x}, t)$ should be regarded as an N-dimensional vector function in a Hilbert space of the N coarse-grained boxes that we also denote by $\Psi(t)$ (Jordan, 1969). In this picture, the state vectors of the system oscillate around a steady state, and therefore the pattern states can be represented by sums of complex exponentials (Holmes et al., 1996). The eigenfunctions are therefore complex, and it is possible that a precursor to a future large earthquake may have a large imaginary part and a small real part, meaning that the precursor might be difficult to detect. This effect would produce a signal with a weak observational amplitude, somewhat similar to the effect produced by interfering non-normal eigenfunctions in Eq. (3).

Given our inability to observe the true dynamics, we therefore seek to define an apparent *pattern dynamics* for the system. Our goal is to define a pattern dynamics operator $P_D(t)$, similar to the pattern evolution operator in Eq. (3). In previous work (Rundle et al., 2000), we conjectured that such an operator can be constructed by the use of the equal-time correlation operator (matrix) d. $d(\boldsymbol{x}, \boldsymbol{y})$ is obtained by cross-correlating the observed real time series $S(\boldsymbol{x}, t)$ and $S(\boldsymbol{y}, t)$ over a time interval $[0, T]$.

EGU

A more rigorous definition of $P_D(t)$ has been developed in Klein et al. (2006)[4], which is found to be related to the inverse of D, D^{-1}. Details of this construction are left to Klein et al. (2006)[4] and future publications.

For the present, we illustrate the general types of patterns revealed by this analysis by plotting eigenvectors of D , which represents the correlation of activity, considering $S(\mathbf{x}, t)$ and $S(\mathbf{y}, t)$ as a Brownian "noise".

To compute the equal-time correlation operator D($\mathbf{x}, \mathbf{y}$), we evaluate:

$$D(\mathbf{x}, \mathbf{y}) \equiv \frac{1}{T} \int_0^T S(\mathbf{x}, t)\, S(\mathbf{y}, t)\, dt \tag{6}$$

If we consider $\mathbf{x}$ to be the spatial coordinate centered on the coarse-grained (box) location $\mathbf{x}_i$, and $\mathbf{y}$ to be the spatial coordinate on the coarse-grained (box) location $\mathbf{x}_j$, then we have the $N{\times}N$ square, symmetric matrix D_{ij}, which can be diagonalized by standard techniques of singular value decomposition (Rundle et al., 2000):

$$D = Q\,\Lambda^2\,Q^T \tag{7}$$

Here Q is an $N{\times}N$ matrix of orthonormal eigenvectors; Q^T is its transpose; and Λ^2 is a diagonal $N{\times}N$ matrix of eigenvalues λ_n^2, n=1,...,N. The eigenvectors $q_n(\mathbf{x})$ comprise the columns of Q. The N positive eigenvalues of D_{ij} are written in Eq. (7) as the square of the diagonal elements of Λ.

4   Numerical simulations and Virtual California

Numerical simulations are needed in the study of driven threshold systems due to the wide range of temporal and spatial scales involved, and because the true dynamics

---

[4]Klein, W., Gulbahce, N., Gould, H., Rundle, J. B., and Tiampo, K. F.: Precursors to earthquake and nucleation, Phys. Rev. Lett., submitted, 2006.

Title Page

Abstract | Introduction

Conclusions | References

Tables | Figures

◀◀ | ▶▶

◀ | ▶

Back | Close

Full Screen / Esc

Printer-friendly Version

Interactive Discussion

[EGU](#)

are fundamentally unobservable. Simulations are typically carried out on computers ranging from workstations to supercomputers, and can be used to determine both the spatial and temporal eigenpatterns that characterize the activity, and the pattern dynamics, or pattern evolution operator $P_D(t)$.

5   Here we give a brief example of this approach using the Virtual California simulation for earthquakes. Virtual California, which was originally developed by Rundle (1988), includes stress accumulation and release, as well as stress interactions between the San Andreas and other adjacent faults. The model is based on a set of mapped faults with estimated slip rates, prescribed long term rates of fault slip, parameterizations of
10   friction laws based on laboratory experiments and historic earthquake occurrence, and elastic interactions. An updated version of Virtual California (Rundle et al., 2001, 2002, 2004, 2006) is used in this paper. The geologic data on average rates of offset in the model is shown in Table 1 (Rundle et al., 2004). The faults in the model are those that have been active in recent geologic history. Earthquake activity data and slip rates
15   on these model faults are obtained from geologic databases of earthquake activity on the northern San Andreas fault. A similar type of simulation has been developed by Ward and Goes (1993) and Ward (1996, 2000). A consequence of the size of the fault segments used in this version of Virtual California is that the simulations do not generate earthquakes having magnitudes less than about $m \approx 5.8$.

20   Virtual California is a backslip model – the loading of each fault segment occurs due to the accumulation of a slip deficit at the prescribed slip rate of the segment. The vertical rectangular fault segments interact elastically, the interaction coefficients are computed by means of boundary element methods (Crouch and Starfield, 1983). Segment slip and earthquake initiation is controlled by a friction law that has its basis
25   in laboratory-derived physics (Tullis, 1996; Karner and Marone, 2000; Rundle et al., 2004). Onset of initial instability is controlled by a static coefficient of friction. Segment sliding, once begun, continues until a residual stress is reached, plus or minus a random overshoot or undershoot of typically 10%. Onset of instability is also possible by means of a stress-rate dependent effect, in that segment sliding can initiate if stress on

EGU

a segment increases faster than a prescribed value due to failure of a nearby segment. Finally, the friction law used in Virtual California also includes a term that promotes a small amount of stable segment sliding as stress increases. This latter term has been shown to promote stress-field smoothing along neighboring segments, offsetting

5 the stress-roughening effects of increasing fault complexity, and allowing larger earthquakes to occur. To prescribe the friction coefficients we use historical earthquakes having moment magnitudes $m{\geq}5.0$ in California during the last ~200 years (Rundle et al., 2004).

Virtual California includes the major strike-slip faults in California and is illustrated

10 in Fig. 1. In this version of the model, Virtual California is composed of 650 fault segments, each of which has a width of 10 km and a depth of 15 km. A much more detailed treatment and explanation of the dynamics and equations solved numerically for Virtual California simulations can be found in (Rundle et al., 2004, 2005, and references therein).

15 An example of results from Virtual California is shown in Figs. 2a, b in which we show two large earthquakes, one reminiscent of the San Francisco earthquake of 1906 (Fig. 2a) on the northern San Andreas fault, and one similar to the Fort Tejon earthquake of 1857 on the southern San Andreas fault near the Big Bend between Fort Tejon and Wrightwood (Fig. 2b). In both Figs. 2a, b, red vertical bars represent "right lateral

20 slip" (opposite side of the fault moves to the right) and blue vertical bars represent "left lateral slip".

It can be seen in Fig. 2a that the earthquake on the Northern San Andreas fault, where most of the slip occurs, also involves triggered slip on the Hayward, Rogers Creek and Maacama faults (these are the faults to the east of – "behind" – the main

25 trace of the San Andreas fault). The dark bar on the San Andreas fault represents the epicentral segment, the segment that was the first to slip in the event. The maximum amplitude of slip, as shown in the figure, is 9.3 m.

Figure 2b shows a large event in southern California similar in extent and magnitude to the 1857 Fort Tejon earthquake. It can be seen that while most of the slip occurs

EGU

on the main trace of the San Andreas fault, where the maximum amplitude of slip is 12.6 m, other triggered slip occurs on the Big Pine fault, the Garlock fault, the San Gabriel fault, and faults in the Mojave desert and Owens Valley to the east. In fact, it is extremely interesting that all of this activity began with initial slip on a small fault in the Mojave desert, as shown by the location of the dark epicentral vertical slip bar.

5 Patterns in Virtual California

We used 10 000 years of simulation data from Virtual California to compute the N=650 spatial patterns of activity for the simulation. These patterns reveal which are the most dominant and important modes of correlated activity, and which are less important. The eigenvectors (spectrum) indicate the fraction of the eigenvectors that are present, on average, in the activity during the simulation. More specifically, $p_n=\lambda_n^2$, is the fraction of eigenvector $q_n(\boldsymbol{x})$ of the orthonormal $N\times N$ matrix $\boldsymbol{Q}$ of Eq. (7) is present, on average, in the activity. Note that $\sum_{n=1}^{N} p_n=1$. Using a frequency interpretation for probability, we can say that on average, over the 10 000 years of simulation data, the probability of finding eigenvector $q_n(\boldsymbol{x})$ in the data is on average p_n.

In Figs. 3a, b, c, d we show the first four orthonormal correlation eigenvectors $q_n(\boldsymbol{x})$, again for the same 10 000 years of simulation data. In these figures, the red and blue bars correspond to locations where the value of $q_n(\boldsymbol{x})$ is significantly different from 0. The heights of the red and blue bars represent the values of $q_n(\boldsymbol{x})$, and can take on values between -1. and $+1$. Red bars represent positive values of $q_n(\boldsymbol{x})$ between 10^{-3} and 1, and blue bars represent negative values of $q_n(\boldsymbol{x})$ between -1 and -10^{-3}. Green dashed lines are locations where $|q_n(\boldsymbol{x})|$ has a value less than 10^{-3}, which is roughly the amplitude of the numerical error. The physical meaning of the red and blue colors for a particular eigenvector $q_n(\boldsymbol{x})$, which represents a particular fundamental pattern of activity is:

EGU

- – Red sites tend to be active when other red sites are active, so that activity at red sites is positively correlated with activity at other red sites;

- – Blue sites tend to be active when other blue sites are active, so that activity at blue sites is positively correlated with activity at other blue sites;

5   – Red sites tend to be inactive when the blue sites are active and vice-versa, so that activity at red sites is negatively correlated with activity at other blue sites.

Figure 3a is an eigenvector that represents the most important pattern of activity in the 10 000 years of simulation data. This pattern of activity comprises p_1=3.5%, on average, of the activity over 10 000 years of simulations. It bears a strong resemblance
10   to Fig. 2b, the 1857-type event. From Fig. 3a, it can be seen that this pattern is associated with correlated activity on the San Andreas, the Garlock and Big Pine, the Northern Mojave, the Owens Valley and Death Valley faults. If one were to expand the pattern of slip in Fig. 2b as a sum of the eigenvectors $q_n(\boldsymbol{x})$, the expansion coefficient $q_1(\boldsymbol{x})$ would represent the most important term.

15   Figure 3b shows the second-most important eigenvector $q_2(\boldsymbol{x})$. Here we primarily see strongly correlated activity on the northern San Andreas, the Hayward-Rogers Creek-Maacama, the Calaveras and Bartlett Springs fault systems. This pattern of activity is seen in 3.1% of the activity over the 10 000 years of simulations. This eigenvector also resembles the event shown in Fig. 2a, the 1906-type event.

20   It is interesting that these first two patterns of activity are effectively decoupled between northern and southern California. The physical explanation for the decoupling is probably related to the existence of the creeping zone of the central San Andreas fault. This zone is the ∼100 km long part of the San Andreas fault just to the north of the large slipped region in Fig. 2b. Earthquakes do not occur in the creeping zone, rather a
25   steady aseismic slip is observed at a rate corresponding to the long-term rate of plate motion across the fault, 35 mm/yr (Table 1). The creeping zone appears to act as a kind of "shock absorber" for the largest events, effectively eliminating the correlation of these events in the north and south.

EGU

Eigenvectors 3 and 4 are shown in Figs. 3c and d. Figure 3c shows a pattern, representing 2.4% of the activity, characterized by correlated slip on the southernmost part of the faults of the San Andreas system, together with slip activity on the eastern Garlock fault. Figure 3d is an interesting pattern, in which a kind of higher "pattern harmonic" of the activity on the faults of the northern San Andreas fault. Comparing Figs. 3b and d, eigenvector 4 (1.8% of the activity) shows an anticorrelation between activity on the extreme northern end of the San Andreas system with the faults near the San Francisco Bay region (refer to Fig. 1 for locations relative to San Francisco). Eigenvector 4 also shows the beginnings of correlations between activity in northern California with activity south of the creeping zone, on the eastern Garlock fault in the Mojave desert. Evidently the decoupling effect of activity in the north and south by the creeping zone of the San Andreas decreases as the higher pattern harmonics appear.

Figure 4 shows the eigenvalue spectrum p_n. Here we plot $\mathrm{Log}_{10}\, p_n$ as a function of $\mathrm{Log}_{10} n$. We observe that there is a region of scaling or power-law behavior at values of n in the interval between $n{\sim}10$ and $n{\sim}200$:

$$\mathrm{Log}_{10}\, p_n \propto -.75\mathrm{Log}_{10} n \,(10 \leq n \leq 200) \tag{8}$$

To understand this, we suppose that we can define a "characteristic wavelength" λ_n for each pattern according to the approximate *ansatz*:

$$\lambda_n \sim \frac{2\pi L}{n} \tag{9}$$

where L represents the linear size (length) of the largest events in the simulations. Then the scaling region shown in Fig. 4 must be an expression of the hierarchical nature of the spatial scale of the patterns generated by the fault system dynamics:

$$p_n \sim \lambda_n^{\alpha} \sim n^{-\alpha} \tag{10}$$

The reason for the particular value of the scaling exponent $\alpha=0.745\pm0.004\approx0.75$ is not at present known, but its value, which is nearly equal to the ratio of integers $3/3$, would lead to the conjecture that it is related to the mean field nature of the dynamics

Pattern dynamics, pattern hierarchies, and forecasting

J. B. Rundle et al.

Title Page

| Abstract | Introduction |

| Conclusions | References |

| Tables | Figures |

| ◀◀ | ▶▶ |

| ◀ | ▶ |

| Back | Close |

Full Screen / Esc

Printer-friendly Version

Interactive Discussion

(Rundle, 1989; Rundle and Klein, 1993; Tiampo et al., 2002a). In mean field dynamics, it is frequently the case that the scaling exponents are ratios of integers (see Klein et al., 2000).

We note that similar types of overall behavior for patterns has been observed in seismicity data (Tiampo et al., 2002b).

6 Conclusions

Forecasting in systems such as ENSO and earthquakes depends on the interpretation of observable space-time patterns, since the true stress-strain rate and stress-strain dynamics cannot be observed. It is likely that similar methods can be used for both systems, based upon the identification of patterns as eigenvectors of a dynamical correlation operator. We note that these are linear descriptions of fundamentally nonlinear dynamical systems. However, there are important examples of of probability distributions for nonlinear systems that are known to obey linear Fokker-Planck equations (Haken, 1983). Moreover, Klein et al. (2006)[4] show that the evolution of patterns in driven threshold systems can be characterized by correlation functions that have the properties discussed above.

We may speculate that hierarchical patterns that are observed in other nonlinear earth systems may be described in by similar methods. For example, it is known that in hydrology, river networks are observed to display scaling patterns that arise from purely local dynamics. These local dynamics include hill slope and topography, surface winds and erosion, and rainfall. Yet these local effects are often the product of long range interactions, i.e., correlation of hill slope and topography, and rainfall patterns over long distances (Turcotte, 1997). Moreover, the tree-like nature of river networks leads also to the conjecture that pattern hierarchies may have a mean field character, inasmuch as tree-like networks are often found to be mean field constructs, such as the Bethe lattice in percolation theory (Stauffer and Aharony, 1994). Understanding how these hierarchies of pattern scales develop and evolve doubtless holds the key to

EGU

forecasting the future dynamical states of these systems.

References

Bowman, D. D., Ouillon, G., Sammis, C. G., Sornette, A., and Sornette, D.: An observational test of the critical earthquake concept, J. Geophys. Res., 103, 24 359–24 372, 1998.

Broomhead, D. S. and King, G. P.: Extracting qualitative dynamics from experimental data, Physica D, 20, 217–236, 1986.

Bufe, C. G. and Varnes, D. J.: Predictive modeling of the seismic cycle of the greater San Francisco Bay region, J. Geophys. Res., 98, 9871–9883, 1993.

Crouch, S. L. and Starfield, A. M.: Boundary Element Methods in Solid Mechanics: with Applications in Rock Mechanics and Geological Engineering, George Allen & Unwin, London, 1983.

Farrell, B.: Optimal excitation of neutral Rossby waves, J. Atmos. Sci., 45, 163–172, 1988.

Frankel, A. F.: Mapping seismic hazard in the Central and Eastern United States, Seismol. Res. Lett., 66, 8–21, 1995.

Garcia, A. and Penland, C.: Fluctuating hydrodynamics and principal oscillation pattern analysis, J. Stat. Phys., 64, 1121–1132, 1991.

Goes, S. D. B. and Ward, S. N.: Synthetic seismicity for the San Andreas Fault, Ann. Geofisica, 37, 1495–1513, 1994.

Haken, H.: Synergetics: An Introduction, Springer-Verlag, Berlin, 1983.

Holliday, J. R., Chen, C. C., Tiampo, K. F., Rundle, J. B., Turcotte, D. L., and Donnellan, A.: A RELM earthquake forecast based on pattern informatics, Seism. Res. Lett., in press, 2006.

Title Page

Abstract | Introduction

Conclusions | References

Tables | Figures

◀ | ▶

◀ | ▶

Back | Close

Full Screen / Esc

Printer-friendly Version

Interactive Discussion

EGU

Holmes, P., Lumley, J. L., and Berkooz, G.: Turbulence, Coherent Structures, Dynamical Systems and Symmetry, Cambridge University Press, Cambridge, UK, 1996.

Jordan, T. F.: Linear Operators for Quantum Mechanics, John Wiley, New York, 1969.

Kagan, Y. Y. and Jackson, D. D.: Probabilistic forecasting of earthquakes, Geophys. J. Int., 143, 438–453, 2000.

Karner, S. L. and Marone, C.: Effects of loading rate and normal stress on stress drop and stick-slip recurrence interval, in: GeoComplexity and the Physics of Earthquakes, edited by: Rundle, J. B., Turcotte, D. L., and Klein, W., Geophysical Monograph, 120, pp. 187–198, American Geophysical Union, Washington, D.C., 2000.

Keilis-Borok, V.: The lithosphere of the earth as a nonlinear system with implications for earthquake prediction, Rev. Geophys., 28, 19–34, 1990.

Kerr, R. A. and Bagla, P.: A seismic murmur of what's ahead for India, Science, 310, 208, 2005.

Keilis-Borok, V., Shebalin, P., Gabrielov, A., and Turcotte, D.: Reverse tracing of short-term earthquake precursors, Phys. Earth Planet. Int., 145, 75–85, 2004.

Klein, W., Anghel, M., Ferguson, C. D., Rundle, J. B., and Martins, J. S. S.: Statistical analysis of a model for earthquake faults with long-range stress transfer, in: GeoComplexity and the Physics of Earthquakes, edited by: Rundle, J. B., Turcotte, D. L., and Klein, W., Geophysical Monograph, 120, pp. 187–198, American Geophysical Union, Washington, D.C., 2000.

Kossobokov, V. G., Keilis-Borok, V. I., Turcotte, D. L., and Malamud, B. D.: Implications of a statistical physics approach for earthquake hazard assessment and forecasting, Pure Appl. Geophys., 157, 2323–2349, 2000.

Lay, T., Kanamori, H., Ammon, C. J., Nettles, M., Ward, S. N., Aster, R. C., Beck, S. L., Bilek, S. L., Brudzinski, M. R., Butler, R., DeShon, H. R., Ekstrom, G., Satake, K., and Sipkin, S.: The great Sumatra-Andaman earthquake of 26 December, 2004, Science, 308, 1127–1133, 2005.

Penland, C. and Sardeshmukh, P.: The optimal growth of tropical sea surface temperature anomalies, J. Climate, 8, 1999–2024, 1995.

Penland, C. and Magorian, T.: Prediction of Nino 3 sea surface termperatures using linear inverse modeling, J. Climate, 6, 1067–1075, 1993.

Penland, C. and Matrosova, L.: Studies of El Nino and interdecadal variability in tropical sea surface temperatures using a non-normal filter, J. Climate, in press, 2006.

Preisendorfer, R. W.: Principal Component Analysis in Meteorology and Oceanography, edited

Pattern dynamics, pattern hierarchies, and forecasting

J. B. Rundle et al.

Title Page

Abstract	Introduction
Conclusions	References
Tables	Figures

|◄ ►|

◄ ►

Back Close

Full Screen / Esc

Printer-friendly Version

Interactive Discussion

EGU

by: Mobley, C. D., Develop. Atmos. Sci., 17, Elsevier, Amsterdam, 1988.

Rundle, J. B.: A physical model for earthquakes, 2, Application to southern California, J. Geophys. Res., 93, 6255–6274, 1988.

Rundle, J. B.: A physical model for earthquakes: 3. Thermodynamical approach and its relation to nonclassical theories of nucleation, J. Geophys. Res., 94, 2839–2855, 1989.

Rundle, J. B. and Klein, W.: Scaling and critical phenomena in a class of slider block cellular automaton models for earthquakes, J. Stat. Phys., 72, 405–412, 1993.

Rundle, J. B., Rundle, P. B., Donnellan, A., and Fox, G.: Gutenberg-Richter statistics in topologically realistic system-level earthquake stress-evolution simulations, Earth Planets Space, 56, 761–771, 2004.

Rundle, J. B., Tiampo, K. F., Klein, W., and Martins, J. S. S.: Self-organization in leaky threshold systems: The influence of near-mean field dynamics and its implications for earthquakes, neurobiology, and forecasting, Proc. Nat. Acad. Sci., USA, 99, 2514–2521., Suppl. 1, 2002a.

Rundle, J. B., Rundle, P. B., Klein, W., Martins, J. S. S., Tiampo, K. F., Donnellan, A., and Kellogg, L. H.: Pure Appl. Geophys., 159, 2357–2381, 2002b.

Rundle, J. B., Rundle, P. B., Donnellan, A., and Fox, G.: Gutenberg-Richter statistics in topologically realistic system-level earthquake stress-evolution simulations, Earth Planets Space, 56, 761–771, 2004.

Rundle, J. B., Rundle, P. B., Donnellan, A., Turcotte, D., Shcherbakov, R., Li, P., Malamud, B. D., Grant, L. B., Fox, G. C., McLeod, D., Yakovlev, G., Parker, J., Klein, W., and Tiampo, K. F.: A simulation-based approach to forecasting the next great San Francisco earthquake, Proc. Nat. Acad. Sci., 102, 15 363–15 367, 2005.

Rundle, J. B., Rundle, P. B., Donnellan, A., Li, P., Klein, W., Morein, G., Turcotte, D. L., and Grant, L.: Stress Transfer in Earthquakes and Forecasting: Inferences from Numerical Simulations, Tectonophysics, 413, 109–125, doi:10.1016/j.tecto.2005.10031, 2006.

Rundle, P. B., Rundle, J. B., Tiampo, K. F., Martins, J. S. S., McGinnis, S., and Klein, W.: Nonlinear network dynamics on earthquake fault systems, Phys. Rev. Lett., 8714, Art. No. 148501, 2001.

Stauffer, D. and Aharony, A.: Introduction to Percolation Theory, Taylor and Francis, Bristol, PA, 1994.

Sykes, L. R. and Jaume, S. C.: Seismic activity on neighboring faults as a long-term precursor to large earthquakes in the San Francisco Bay area, Nature, 348, 595–599, 1990.

Tiampo, K. F., Rundle, J. B., McGinnis, S., Gross, S., and Klein, W.: Mean field threshold

Pattern dynamics, pattern hierarchies, and forecasting

J. B. Rundle et al.

Title Page	
Abstract	Introduction
Conclusions	References
Tables	Figures
◄◄	►►
◄	►
Back	Close
Full Screen / Esc	

Printer-friendly Version

Interactive Discussion

EGU

systems and phase dynamics: An application to earthquake fault systems, Europhys. Lett., 60, 481–487, 2002a.

Tiampo, K. F., Rundle, J. B., Gross, S. J., McGinnis, S., and Klein, W.: Eigenpatterns in southern California seismicity, J. Geophys. Res., 107, B12, 2354, doi:10.1029/2001JB000562, 2002b.

Tiampo, K. F., Rundle, J. B., Klein, W., Martins, J. S. S., and Ferguson, C. D.: Ergodic dynamics in a natural threshold system, Phys. Rev. Lett., 91, 238 501(1–4), 2003.

Travis, J.: Scientists' fears come true as hurricane floods New Orleans, Science, 309, 1656–1659, 2005.

Tullis, T. E.: Rock friction and its implications for earthquake prediction examined via models of Parkfield earthquakes, Proc. Nat. Acad. Sci. USA, 93, 3803–3810, 1996.

Turcotte, D. L.: Fractals and Chaos in Geology and Geophysics, 2nd Edition, Cambridge University Press, Cambridge, UK, 1997.

Vautard, R. and Ghil, M.: Singular spectrum analysis in nonlinear dyanmics, with applications to paleoclimate time series, Physica D, 35, 395–424, 1989.

Ward, S. N.: An application of synthetic seismicity in earthquake statistics: the Middle America Trench, J. Geophys. Res., 97, 6675–6682, 1992.

Ward, S. N.: A synthetic seismicity model for southern California: Cycles, probabilities, hazards, J. Geophys. Res., 101, 22 393–22 418, 1996.

Ward, S. N.: San Francisco Bay Area earthquake simulations: A step toward a standard physical earthquake model, Bull. Seis. Soc. Am., 90, 370–386, 2000.

Ward, S. N. and Goes, S. D. B.: How regularly do earthquakes recur – A synthetic seismicity model for the San Andreas fault, Geophys. Res. Lett., 20, 2131–2134, 1993.

Title Page

Abstract | Introduction

Conclusions | References

Tables | Figures

◄◄ | ►►

◄ | ►

Back | Close

Full Screen / Esc

Printer-friendly Version

Interactive Discussion

EGU

Table 1. Segments and geologic rates of offset for the modified version of VC 2001 used in Figs. 1–4.

Fault or Fault System Name	Segment Nos. Begin	End	Chart Distance (km) Begin	End	Average Slip Rate (mm/yr)
Bartlett Springs	0	7	0.0	84.7	6
Calaveras	8	22	84.7	238.9	15 (8–>17) 6 (18–>22)
Collayomi	23	25	238.9	266.8	.6
Concord-Green Valley	26	31	266.8	322.2	6
Death Valley	32	55	322.2	569.6	5 (32–>49) 4 (50–>55)
Garberville-Briceland	56	59	569.6	609.2	9
Greenville	60	66	609.2	682.2	2
Hayward	67	77	682.2	793.3	9 (67–>74) 3 (75–>77)
Hunter Mtn.-Saline Val.	78	84	793.3	861.3	2.5
Hunting Creek-Berryessa	85	90	861.3	920.3	6
Lake Mountain	91	93	920.3	953.7	6
Maacama	94	111	953.7	1133.3	9
Monterey Bay-Tularcitos	112	119	1133.3	1213.6	.5
Ortigalita	120	126	1213.6	1280.1	1
Owens Valley	127	138	1280.1	1401.6	1.5
Palo Colorado-Sur	139	146	1401.6	1479.8	3
Panamint Valley	147	156	1479.8	1584.5	2.5
Quien Sabe	157	158	1584.5	1607.6	1
Rinconada	159	177	1607.6	1796.9	1
Rodgers Creek	178	183	1796.9	1858.9	9
Round Valley	184	189	1858.9	1914.3	6
San Gregorio	190	198	1914.3	2003.3	5
Sargent	199	203	2003.3	2056.0	3
West Napa	204	206	2056.0	2085.9	1
White Mountains	207	216	2085.9	2186.5	1
San Andreas North	217	263	2186.5	2653.6	24 (217–>248) 17 (249–>263)
San Andreas Creeping	264	273	2653.6	2751.3	34
San Andreas South	274	335	2751.3	3330.7	34 (274–>298) 30 (299–>312) 24 (313–>321) 25 (322–>335)
San Jacinto	336	364	3330.7	3622.1	12 (336–>352) 14 (353–>364)
Elsinore	365	388	3622.1	3857.5	3 (365–>368) 5 (369–>384) 4 (385–>388)

EGU

Table 2. Continued.

Fault or Fault System Name	Segment Nos. Begin	End	Chart Distance (km) Begin	End	Average Slip Rate (mm/yr)
Imperial Valley	389	406	3857.5	4020.0	30
Laguna Salada	407	416	4020.0	4118.5	4
Garlock		417	440	4118.5	4353.0–5 (417–>426)–7 (427–>440)
Palos Verdes	441	447	4353.0	4428.6	3
Santa Cruz Island	448	452	4428.6	4481.9	–3
Brawley	453	457	4481.9	4533.8	25
Santa Monica	458	468	4533.8	4653.3	–3
Cleghorn	469	470	4653.3	4676.4	–3
Tunnel Ridge	471	472	4676.4	4695.6	–1.3
Helendale	473	481	4695.6	4781.7	.8
Lenwood-Lockhart	482	499	4781.7	4955.2	.8
Pipes Canyon	500	501	4955.2	4970.8	.7
Gravel Hills-Harper	502	509	4970.8	5051.2	.9
Blackwater	510	516	5051.2	5113.0	2
Camp Rock-Emerson	517	527	5113.0	5227.2	1 (517–>524) .6 (525–>527)
Homestead Valley	528	530	5227.2	5254.4	.6
Johnson Valley	531	536	5254.4	5320.4	.6
Calico-Hidalgo	537	549	5320.4	5455.5	1 (537) 1.7 (538) 2.6 (539–>545) .6 (546–>549)
Pisgah-Bullion	550	562	5455.5	5571.2	1
Mesquite Lake	563	564	5571.2	5592.2	1
Pinto Mountain	565	573	5592.2	5676.0	–1
Morongo Valley	574	574	5676.0	5690.6	–.5
Burnt Mountain		575	576	5690.6	5707.6.6
Eureka Peak	577	578	5707.6	5725.8	.6
Hollywood-Raymond	579	582	5725.8	5763.7	–1 (579–>580) –.5 (581–>582)
Inglewood-Rose Cyn	583	604	5763.7	5979.2	1 (583->590) 1.5 (591->604)
Coronado Bank	605	623	5979.2	6179.5	3
San Gabriel	624	637	6179.5	6310.8	3 (624–>628) 2 (630–>633) 1 (634–>637)
Big Pine	638	644	6310.8	6379.5	–4
White Wolf	645	649	6379.5	6427.6	–5

Pattern dynamics, pattern hierarchies, and forecasting

J. B. Rundle et al.

Title Page

Abstract | Introduction

Conclusions | References

Tables | Figures

|◀ | ▶|

◀ | ▶

Back | Close

Full Screen / Esc

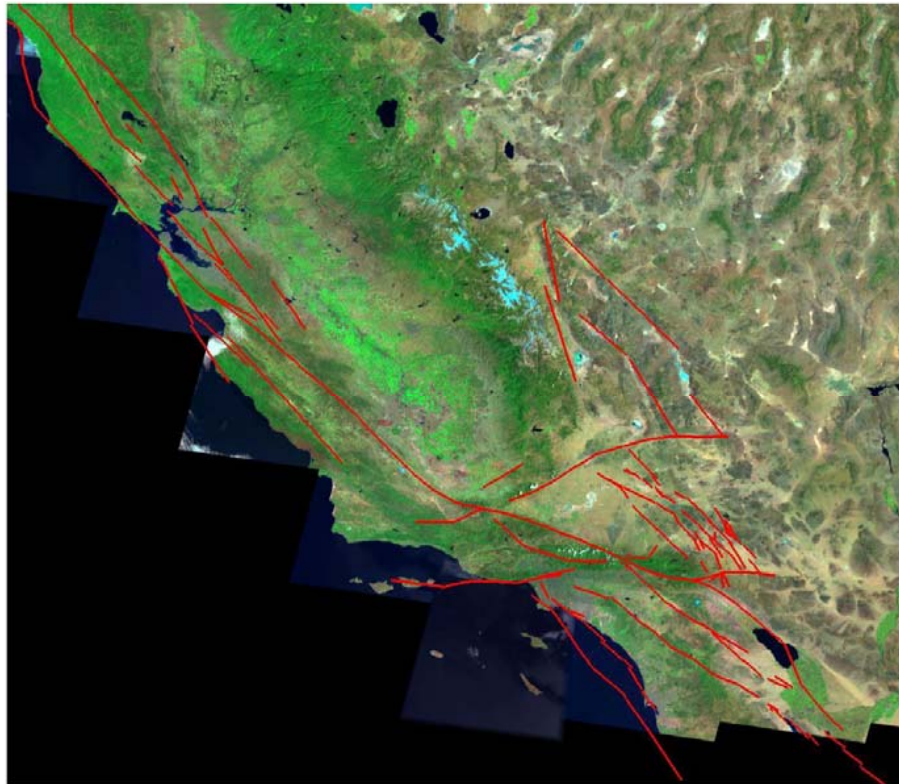Printer-friendly Version

Interactive Discussion

EGU

Fig. 1. Fault segments making up Virtual California. The model has 650 strike-slip fault segments, each approximately 10 km in length along strike and 15 km in depth.

Event Time: 265375. Years
Maximum Slip: 9.317 Meters
RED => RIGHT Lateral Slip
BLUE => LEFT Lateral Slip
DARK => Epicenter

Event Time: 266370. Years
Maximum Slip: 12.65 Meters
RED => RIGHT Lateral Slip
BLUE => LEFT Lateral Slip
DARK => Epicenter
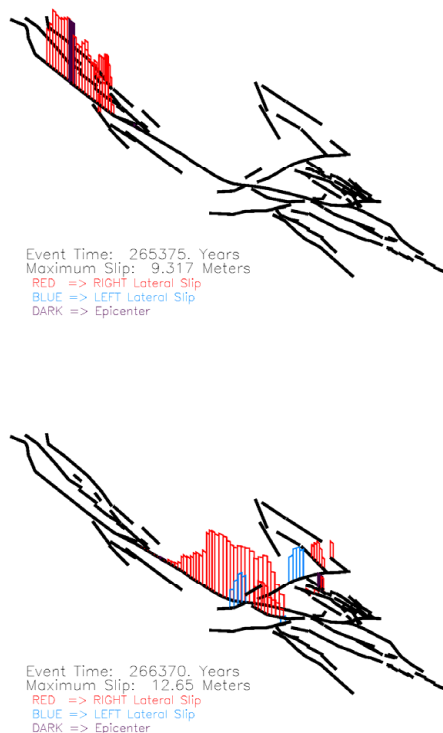
Fig. 2. Illustration of simulated earthquakes on the San Andreas fault. Two large earthquakes are shown. Panel **(a)** is an event that is reminiscent of the San Francisco earthquake of 1906 on the northern San Andreas fault. Panel **(b)** is an event that is similar to the Fort Tejon earthquake of 1857 on the southern San Andreas fault near the Big Bend between Fort Tejon and Wrightwood.

EGU

Eigenvector: 1
Probability : 0.035

Eigenvector: 2
Probability : 0.031

Eigenvector: 3
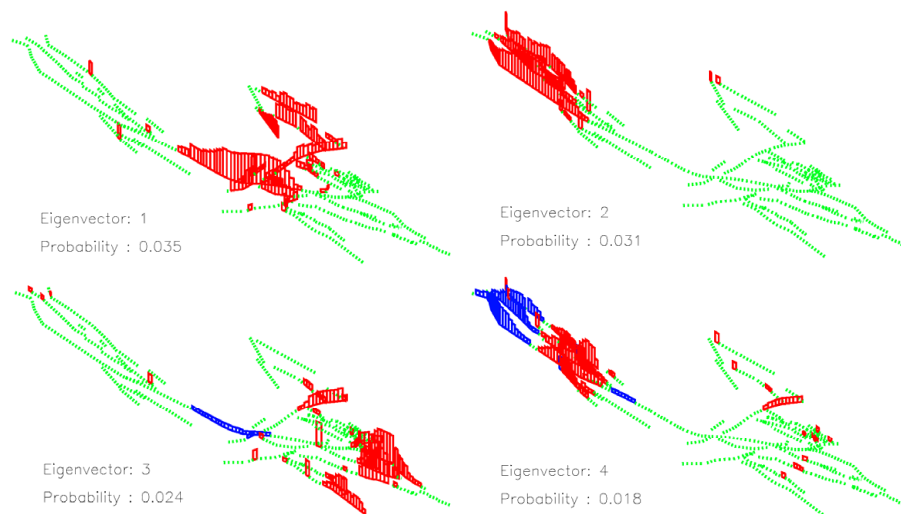Probability : 0.024

Eigenvector: 4
Probability : 0.018

Fig. 3. This figure shows the first (and most important) four correlation eigenvectors for 10 000 years of simulation data. The color-coding of the vertical bars is that: 1) Red sites tend to be active when other red sites are active, so that activity at red sites is positively correlated with activity at other red sites; 2) Blue sites tend to be active when other blue sites are active, so that activity at blue sites is positively correlated with activity at other blue sites; 3) Red sites tend to be inactive when the blue sites are active and vice-versa, so that activity at red sites is negatively correlated with activity at other blue sites.
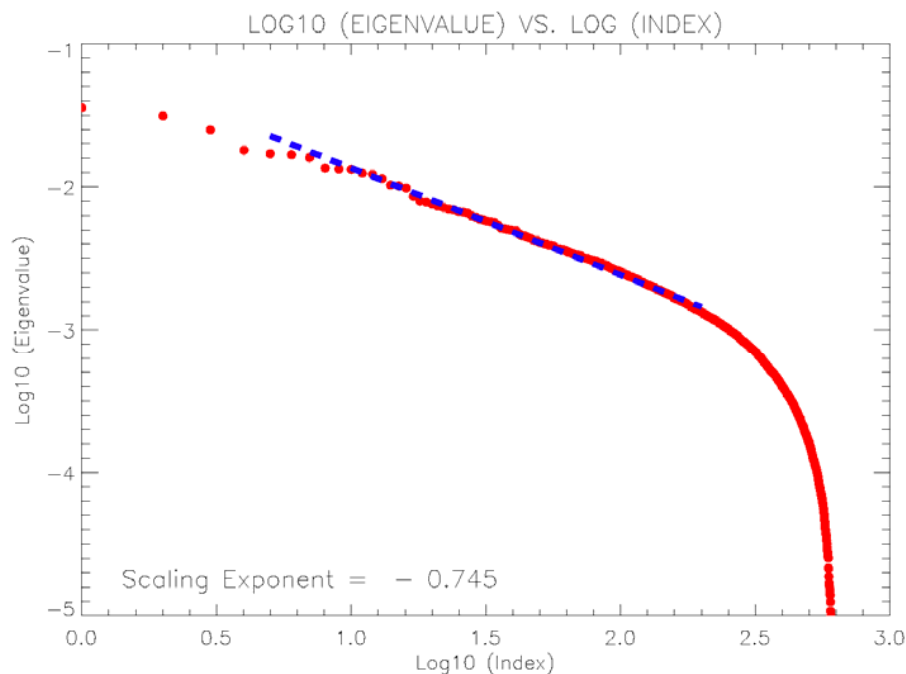
EGU

Fig. 4. Plot of the eigenvalue spectrum p_n on a log-log plot. $\text{Log}_{10} p_n$ is plotted as a function of $\text{Log}_{10} n$, where n is the index number of the eigenvector ($n=1$ has the largest value of p_n, and the rest are ordered by descending values of p_n).

Title Page

Abstract   Introduction

Conclusions   References

Tables   Figures

◄◄   ►►

◄   ►

Back   Close

Full Screen / Esc

Printer-friendly Version

Interactive Discussion